Measurements of Muon and Muon-Derived Fluxes Using Gadolinium-Doped Liquid Scintillator at the China Jinping Underground Laboratory*

Xiao-Yu Peng,[1] Chang-Hao Fang,[1] Shin-Ted Lin,[1, †] Shu-Kui Liu,[1, ‡] Han-Yu Li,[1] Qian-Yun Li,[1] Ren-Ming-Jie Li,[1] Yu Liu,[1] Hao-Yu Shi,[1] Qin Wang,[1] Hao-Yang Xing,[1] Yu-Lu Yan,[1] Li-Tao Yang,[2] Qian Yue,[2] and Jing-Jun Zhu[1]

[1]*College of Physics, Sichuan University, 610065 Chengdu, China*
[2]*Key Laboratory of Particle and Radiation Imaging (Ministry of Education) and*
Department of Engineering Physics, Tsinghua University, 100084 Beijing, China

We present the results of an experiment conducted to measure cosmic-ray muons and muon-induced fluxes at the China Jinping Underground Laboratory. Utilizing a 28-liter 0.5% gadolinium-doped liquid scintillator detector, which operated stably for 412 days in a 1-meter-thick polyethylene shielding, we reconstructed saturated signal pulses and pulse shape discrimination to facilitate measurements across a range starting from 0.2 MeV. The event rates incorporating mountain geometry effects for cosmic rays and their induced particles are derived. The experimental results show that cosmic ray muon flux is $(4.06 \pm 0.57) \times 10^{-10}$ cm^{-2} s^{-1}, muon-induced electron flux is $(0.72 \pm 0.1) \times 10^{-10}$ cm^{-2} s^{-1}, and the upper limit of the muon-induced neutron flux is 3.44×10^{-10} cm^{-2} s^{-1}. They indicated that no significant excess is observed at a 90% confidence-level, particularly no muon-derived neutrons above 10 MeV is detected.

Keywords: Neutron detector, Cosmic ray, Muon flux, Saturated signals, Signal reconstruction

I. INTRODUCTION

In rare-event detection experiments targeting dark matter particles [1, 2], neutrinoless double-beta decay [3, 4], and neutrino property studies [5], cosmic-ray muons represent a critical background background. Their high penetration capacity enables them to traverse multi-kilometer rock overburdens, directly interacting with detector to contaminating rare-event signals [6]. Additionally, high-energy muons can interact with various materials, producing secondary particles, including muon-induced neutrons and electrons. Among these, neutral muon-induced neutrons pose a particularly significant threat. For example, in the low-energy region, it becomes challenging to distinguish between the signals from neutrons and those from dark matter particles (WIMPs) colliding with nucleons [7]. The gamma background from the inelastic scattering of neutrons can obscure neutrinoless double-beta decay events, while signals from neutron elastic scattering may interfere with neutrino signals [8]. As a result, rare event experiments are typically conducted in underground laboratories, where several kilometers of rock provide effective shielding from cosmic-ray muons.

The world's underground laboratories with depths exceeding 2000 meters include the China Jinping Underground Laboratory (CJPL) (2400 meters) [9, 10] and Canada's Sudbury Neutrino Observatory (SNO) (2000 meters) [11], where the cosmic-ray muon flux is as low as 10^{-10} cm^{-2} s^{-1}. The SNO laboratory is situated in a shaft oriented vertically to the surface. Although it provides effective shielding from cosmic-ray muons coming from all directions, access to the labora-

tory requires the use of an elevator. The CJPL, located in the Jinping Tunnel in Sichuan Province, China, is currently the deepest underground laboratory in the world, with over 1,500 meters of rock covering the facility and a maximum vertical rock depth of up to 2,400 meters. The thick rock surrounding the laboratory creates an environment with an exceptionally low background level throughout the facility. Nevertheless, the backgrounds from cosmic-ray muons and muon-induced neutrons remain non-negligible, making it essential to measure their flux at the CJPL.

For cosmic-ray muons, Wu et al. used a plastic scintillator telescope to measure muons in the vertical direction. The first measured cosmic ray flux, without applying angular corrections, was $(2.0 \pm 0.4) \times 10^{-10}$ cm^{-2} s^{-1} [12]. Guo et al. carefully considered the geometric structure of the mountain and corrected for the detector's acceptance angle, thereby obtaining a more accurate measurement of the cosmic-ray flux, which was $(3.53 \pm 0.22$ (stat.) ± 0.07 (syst.)$) \times 10^{-10}$ cm^{-2} s^{-1} [13].

The flux of muon-induced neutrons is typically one order of magnitude lower than that of cosmic-ray muons [14]. For neutron detection, a 0.5% gadolinium-doped liquid scintillator (Gd-LS) detector has been engineered [15, 16]. Previous experiments have demonstrated that Gd-LS detector exhibits excellent n-γ discrimination and neutron detection capabilities [15, 17, 18]. This is achieved using the pulse shape discrimination (PSD) method [19, 20]. The underlying mechanism stems from distinct energy deposition patterns: neutron-induced nuclear recoils generate signals with prolonged decay tails compared to gamma-induced electronic recoils, enabling discrimination via an integral-dependent discriminating factor (Dis factor). Neutron detection is achieved by analyzing the fast signal, slow signal, and the time interval between them. In particular, neutrons entering the Gd-LS detector generate fast signals caused by recoil nuclei through elastic scattering. As neutrons lose energy and slow down, they may be captured by gadolinium nuclei, which results in the emission of a set of gamma rays with an energy of ap-

proximately 8 MeV, producing the slow signals. To exclude coincident events caused by gamma background, a neutron event is considered valid only if the time interval between the fast and slow signals is greater than 2 μs and less than 40 μs.

Additionally, neutrons originating from environmental (α, n) reactions and U/Th decay must be distinguished from muon-induced neutrons [21–27]. The former two types of neutrons typically originate from the rock surrounding the laboratory and the materials of the detector itself, with their energies generally below 10 MeV. To shield these neutrons from the rock, a 1-meter-thick polyethylene (PE) room had been constructed. Furthermore, based on the Gd-LS detector and the PSD method, Du et al. obtained neutron energy spectrum measurements in the 1 to 10 MeV range within the CJPL Phase I laboratory hall and the PE room [15]. These measurements were conducted using the Gd-LS detector and the SAND-II algorithm to unfold the neutron spectrum. The results indicated that the neutron flux in the CJPL Phase I laboratory hall was $(1.51 \pm 0.03 \text{ (stat.)} \pm 0.10 \text{ (syst.)}) \times 10^{-7}$ cm^{-2} s^{-1}, while in the PE room, it was $(4.9 \pm 0.9 \text{ (stat.)} \pm 0.5 \text{ (syst.)}) \times 10^{-9}$ cm^{-2} s^{-1}. They provided valuable assessments of neutrons in the laboratory, facilitating the application of the Gd-LS detector for ultra-low flux measurements (10^{-11} cm^{-2} s^{-1}). To obtain the source of neutron background in the PE room, Zhong et al. employed a genetic algorithm to optimize the energy spectral continuum, thereby enabling the identification of the U-Th content in the material and determining the source and yield of the primary neutrons [18, 28]. The results indicated that 92.5% of the neutrons in the polyethylene room originated from the aluminum protection plates near the detector, which were found to have a high thorium contamination of 1421.6 ± 171.1 (*μg/kg*).

The muon-induced neutrons originate from cosmic-ray muons, their energies are higher than those of environmental neutrons [29–31]. This enables the energy threshold (above 10 MeV) to effectively distinguish muon-induced neutron events from environmental neutrons and the ambient background. Moreover, high-energy events (above 10 MeV) may not only be attributed to muon-induced neutrons, but also to cosmic-ray muons themselves and muon-induced electrons. Therefore, the PSD method is employed in this study to differentiate between particle types. However, due to the limitations of the DAQ range, higher-energy events interacting with the scintillator produce output signals that saturate, exceeding the DAQ's range. This results in nonlinearities, causing the loss of information in the signals. Therefore, reconstructing saturated signals is essential for achieving accurate measurements of the neutron energy spectrum and cosmic-ray muon fluxes in the high-energy range.

This study analyzes data acquired over 412 days of stable operation from a 28-liter Gd-LS detector in the PE room. The dataset underwent comprehensive signal screening to identify saturation events, with a function-fitting method implements to reconstruct high-energy events (above 10 MeV). To characterize the spectral composition of muon-induced interactions above 10 MeV, Geant4 simulations [32] incorporating mountain overburden geometry are performed, modeling cosmic-ray muon interactions across the full Gd-LS detector volume to determine detection efficiency profiles. Recoil energy analysis employs distinct strategies for low- and high-energy regimes: low-energy processing accounted for neutron moderation and absorption to suppress environmental neutron backgrounds, while high-energy saturated signal reconstruction extended the detector's dynamic range, enhancing precision in underground neutron and muon flux measurements.

II. EXPERIMENTAL DATA PROCESSING

A. Saturation events screening

The Gd-LS detector, located in the CJPL PE room, is a cylindrical detector with a diameter of 0.3 m and a length of 0.4 m. It is filled with 28-liter of EJ-335 liquid scintillator contained in a quartz glass vessel with a thickness of only 4 mm. The scintillator is doped with 0.5% of the total mass of gadolinium. The quartz glass vessel is coated with a PTFE reflective layer on its sides to enhance photon collection efficiency. Hamamatsu R5912-02 photomultiplier tubes (PMTs) are attached to both ends of the vessel, providing double-ended readout for signal collection. Additionally, lead plates, aluminum plates, and PE block shields surround the detector, and the entire experimental setup is positioned in one corner of the PE room.

Neutrons and gamma rays in the environment typically have energies below 10 MeV [33], and their full signals can be measured by the Gd-LS detector. The high energy of the surviving muons (with an average energy of 340 GeV) generates significantly large signals when they and their derivatives are detected. However, due to the parameters set for the DAQ system, the maximum amplitude of the signal waveform, including the baseline, that can be displayed is limited to 244.5. Signals with amplitudes exceeding this threshold are truncated. Previous studies have shown that events below 10 MeV can be recorded successfully [15], while events above 10 MeV mostly exhibit saturation events. To reconstruct saturated events, function-fitting method is used. Additionally, an artificial neural network reconstruction is performed, and the results confirmed that the method is satisfactory.

In this study, data collected over 412 days of stable detector operation are analyzed. This includes all signals that were clearly distinguishable from noise, with stable trigger rates, baselines, and baseline fluctuations.

B. Saturation signal events reconstruction by function-fitting method

The saturation-induced signal truncation caused by the DAQ system's dynamic range limitation leads to irreversible loss of both complete waveform morphology and charge integral data. As the charge integral serves as a critical parameter directly proportional to both energy deposition and the Dis factor of detection events, precise reconstruction of saturated

signals becomes imperative for comprehensive waveform recovery.

It is hypothesized that signal waveforms with different amplitudes would exhibit analogous shape characteristics. To validate this hypothesis, artificial neural network (ANN) methodology is employed [34]. This investigation utilizes a generalized radial basis function (GRBF) neural network, a topology previously validated for robust signal reconstruction performance [34, 35]. Four amplitude domains were designated as training cohorts: 50-100, 100-150, 150-200, and 200-saturation (244.5), with respective training sets containing 10,000, 10,000, 10,000, and 88 events. Crucially, all training samples underwent randomized selection from detection datasets to ensure statistical representativeness, with the final cohort's reduced population reflecting natural amplitude distribution sparsity. The top panel of Fig. 1 demonstrates neural network outputs through characteristic scatter distributions corresponding to each amplitude domain: black inverted triangles (50-100), pink squares (100-150), purple circles (150-200), and blue pentagrams (200-saturation). These clustered patterns substantiate the waveform similarity hypothesis across amplitude variations.

Moreover, parallel reconstruction efforts employs function-fitting method to reconstruct the saturated signal. The red curves in the top panel of Fig. 1 represent the results of fitting all points of the neural network output using a fitting function that can be expressed as Eq. (1), where p_1, p_2, and p_3 are the fitting parameters, respectively represent the amplitude at the peak, the time at the peak, and the half-height width. The bottom panel of Fig. 1 illustrates the outcome of reconstructing one of the saturated signals using this function. The black scatter plot represents the original data, the red curve is the fitted curve, and 244.5 is the limit of DAQ dynamic range. The two plots in Fig. 1 illustrate the validation of this function in approximating the morphological characteristics of the waveform. However, at low amplitudes, the function largely aligns with the waveform features, while at higher amplitudes, it exhibits some bias.

$$A = p_1 \times exp(-exp(-z) - z + 1), \quad z = \frac{x - p_2}{p_3}. \quad (1)$$

C. Analysis of the bias value of the function fitting

To quantify systematic deviations introduced by the fitting function during waveform reconstruction, we establish two distinct bias categories for comprehensive error analysis. Specifically, this analysis focuses on the reconstructed charge integral bias of physical events, which is calculated based on statistical ensembles of numerous events processed through the fitting procedure. Notably, parameter estimation errors in the fitting process are not treated separately, since these errors have already been inherently incorporated into the aforementioned statistical treatment and consequently contribute as inherent components to the observed charge integral bias.
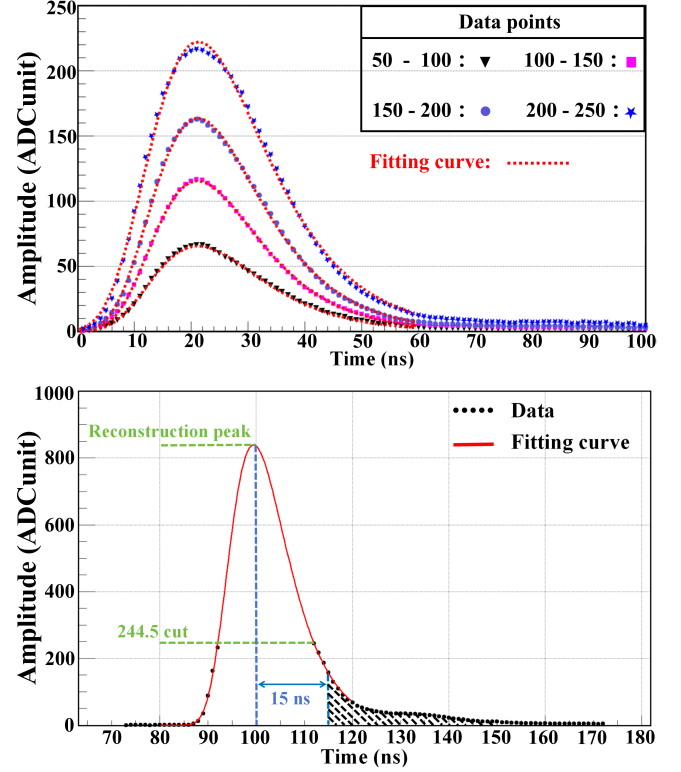

Fig. 1. Top:The ANN outputs the results of four different amplitude waveforms and the fitting of these results using function. Bottom: The function predicts the reconstruction of saturated signal events.

The first type of bias is that the Eq. (1) does not precisely align with the actual waveform, resulting in bias when fitting waveforms with larger amplitudes. The analysis framework utilizes unsaturated signals as baseline references across four amplitude domains: 50-100, 100-150, 150-200, and 200-saturation (244.5). Quantitative evaluation of charge integral bias magnitude across these amplitude ranges enables systematic uncertainty estimation for saturated signal reconstruction. In addition, the following Eq. (2) is defined to describe the first type bias. Where Q_f is the integral under the model of the fitting function and Q_r is the area integral of the real waveform. $Bias$ denotes the degree of bias of the modeled integral of the fitted function from the actual integral of the real waveform.

Fig. 2(a) presents the amplitude-dependent bias distribution through color-coded histograms corresponding to the four amplitude ranges. The inset below depicts the expectation and standard deviation resulting from the fitting using a Gaussian function. As illustrated in Fig. 2(a), the integral bias of the waveforms fitted using this function are all below 0.006 (0.6%), with this value tending to decrease as the amplitude of the waveforms increases. Given that the integral bias in fitting waveforms with the largest known range of amplitudes (200 to saturation) is 0.0023 and follows a decreasing trend, it can be posited that the first type of bias for fitting saturated signals using this function is 0.0023. Therefore, this systematic analysis confirms that the first type of bias remains within
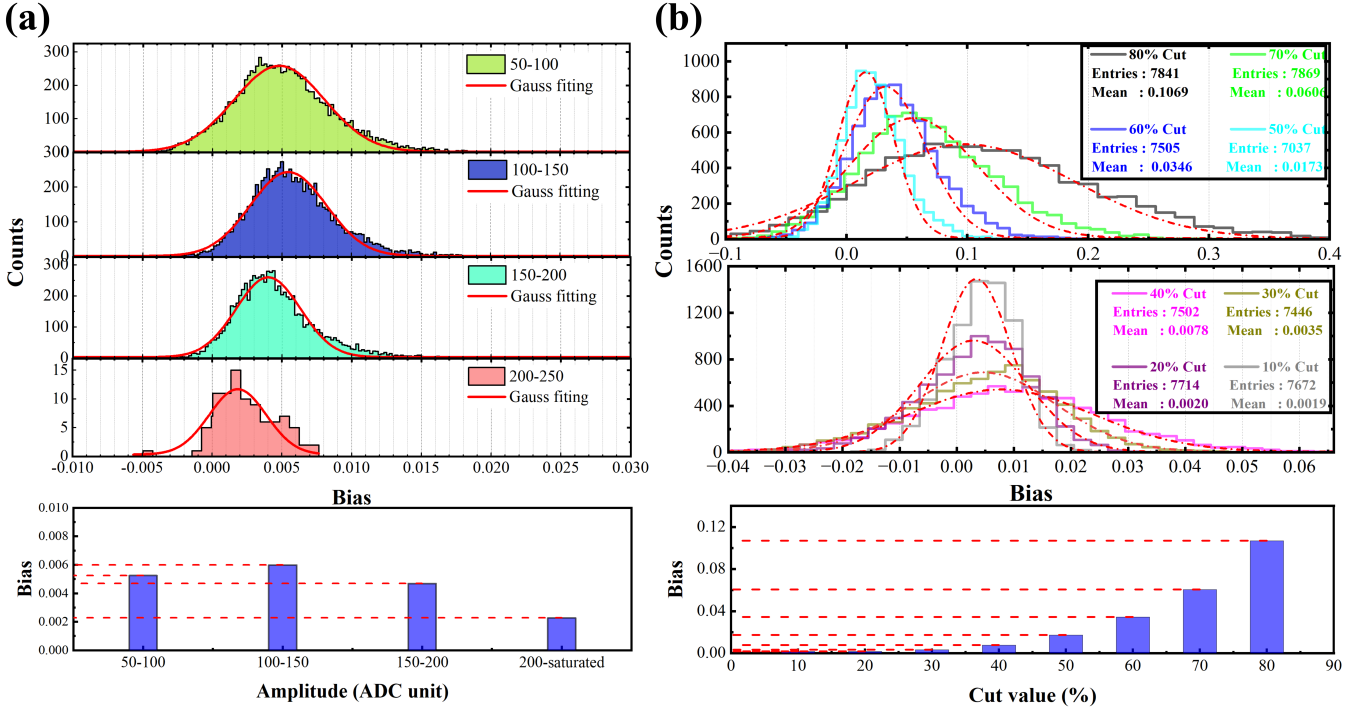
Fig. 2. The first type of bias (**a**) and the second type of bias (**b**) estimates for the function fitting. The insets at the bottom show their statistical information of mean value.

acceptable thresholds for practical applications, justifying the neglect of such biases in subsequent analyses.

$$Bias = \frac{Q_f - Q_r}{Q_r}. \qquad (2)$$

$$Cut = \frac{A - 244.5}{A} \times 100\%. \qquad (3)$$

Furthermore, the second type of bias arises from the prediction errors in reconstructing saturated signals, where signal saturation causes the loss of information. The larger the amplitude of the saturated signal, the more significant the cutoff, leading to a greater loss of information, which in turn introduces bias into the reconstruction process.

Before discussing this bias, the *Cut* value is defined to represent the extent of the cutoff in the signal. This can be expressed by Eq. (3). In this context, *244.5* represents the DAQ dynamic range limit, and *A* denotes the expected peak value following the fitting process. A larger *Cut* value corresponds to a greater portion of the signal being cutoff, while a smaller *Cut* value indicates a smaller cutoff. For example, a waveform with an 80% *Cut* has an original amplitude so large that 80% is truncated by the DAQ dynamic range, leaving only 20% of the actual amplitude. Conversely, a waveform with a 10% *Cut* is just above the DAQ dynamic range, preserving most of its original waveform. To quantify the bias between the integral of the actual and reconstructed waveforms, an *Artificial Cut (AC)* is applied to waveforms over a known

amplitude range. The *AC* introduces a loss of waveform information analogous to the *Cut* previously defined. The selected waveforms have an amplitude range of 100 to 150, which provides a sufficient number of signal events for an accurate fit function. These waveforms are cutoff between 10% and 80%, with 10,000 events considered for each Cut value. This range represents the potential degree of *Cut* for the saturated signals detected. The integral bias is estimated in a manner similar to the first type of bias calculation, as illustrated in Eq. (2). The results are presented in Fig. 2(b). The histograms in Fig. 2(b) illustrate the distribution of the integral bias for different *Cut* values, with the red dashed lines representing the Gaussian fitting curve. The bottom inset in Fig. 2(b) shows the Gaussian fit to the mean value. As observed, a larger *Cut* value leads to a larger bias and a wider distribution. These results corroborate our hypothesis that reconstructing a large-amplitude signal waveform introduces a greater deviation than reconstructing a low-amplitude signal waveform. For an 80% *Cut*, the bias value is 10.7%, whereas for a 10% Cut, the bias value is 0.2%. Therefore, we conclude that this function significantly affects waveform reconstruction, and its reconstruction bias must be considered in both the energy and Dis factor when reconstructing saturated signal events.

D. Results of reconstruction

Following the completion of the evaluation of the bias, the reconstruction of the saturated signal events is performed.
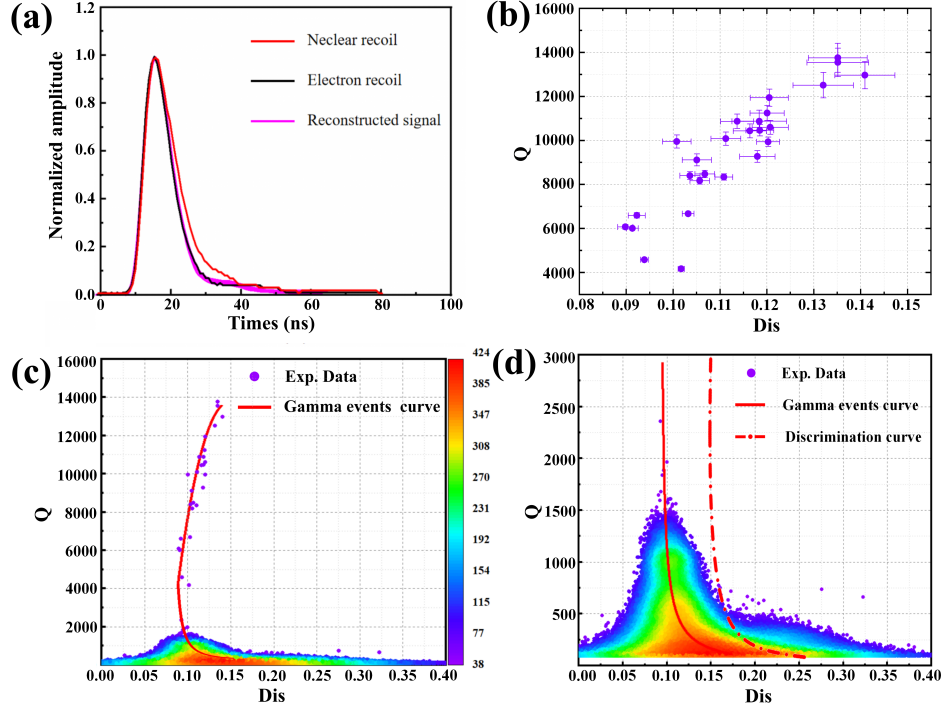
Fig. 3. Waveform discrimination for reconstruction of saturated signal events. (a): Waveform morphology comparison between reconstructed events and reference templates of electronic recoil and nuclear recoil with amplitude-normalized profiles. (b): Q vs Dis distribution for reconstructed events. (c): Two-dimensional Q-Dis distribution into high-energy (Q above 2000) and low-energy (Q below 2000) regions. (d): Two dimensional Q-dis in low-energy region (Q below 2000).

The correction factor (*CF*) is defined as $CF=1-bias$. The charge integral after waveform reconstruction is defined by the following Eq. (4), in which CF represents the correction factor accounting for $Bias$. The Gd-LS detector utilized in the study adopts a double-ended readout of the signals, whereby the light signals are acquired through two PMTs at the front and back of the detector. Consequently, all signals exhibit two waveforms. The geometric mean Q_{total} is defined to describe the total charge integral as shown in Eq. (5). In this instance, the charge integral of the signal, represented by Q_{total}, is defined as the sum of the charge integrals of the two waveforms, represented by Q_1 and Q_2. Dis factor is calculated values through Eq. (6), where Q_{1part} and Q_{2part} are the integrated area 15 ns backward after the peak, as shown at the bottom of Fig. 1. The error transfer equation is utilized to calculate the errors of the total Q_{total} and Dis factors.

$$Q = CF \times Q_f. \qquad (4)$$

$$Q_{total} = \sqrt{Q_1 \times Q_2}. \qquad (5)$$

$$Dis = \frac{Q_{1part} + Q_{2part}}{Q_1 + Q_2}. \qquad (6)$$

Fig. 3 illustrates the results of the processing of the saturation signal events. Fig. 3(a) illustrates the comparison between the reconstructed waveforms of the saturated signal events and the neutron recoil waveforms and electron recoil waveforms. As illustrated in Fig. 3(a), the reconstructed saturated signal events tend to the electron recoil waveform in terms of waveform pulse shapes, exhibiting a significant distinction from the neutron events. Fig. 3(b) illustrates the two-dimensional distribution between Dis and Q, which highlights the characteristics of saturation signal events with Dis less than 0.14. Fig. 3(c) and Fig. 3(d) illustrate the two-dimensional density plot of Dis for the low-energy region of the events. Given the presence of both gamma and neutron events in the environment, the charge integral bin values are separated, and a double Gaussian fit is applied to the Dis count distribution. This fit is used to derive discrimination curves for the two signal regions. The curves are then extended to higher energy regions, as shown by the red dotted line in Fig. 3(d). Additionally, the two fitted curves are combined to predict the range of gamma signal events and cosmic ray signal events from the environment. Specifically, the red curve with Q values below 4000 represents the approximate trend of gamma signal events, while the red curve above 4000 indicates the trend of cosmic ray events.

Finally, the number of events identifies as saturations following the processing of all experimental data is 26. We use Dis = 0.15 as the criterion for determining neutron nuclear recoil events and gamma events. Therefore, 26 saturation events are considered gamma-like events.
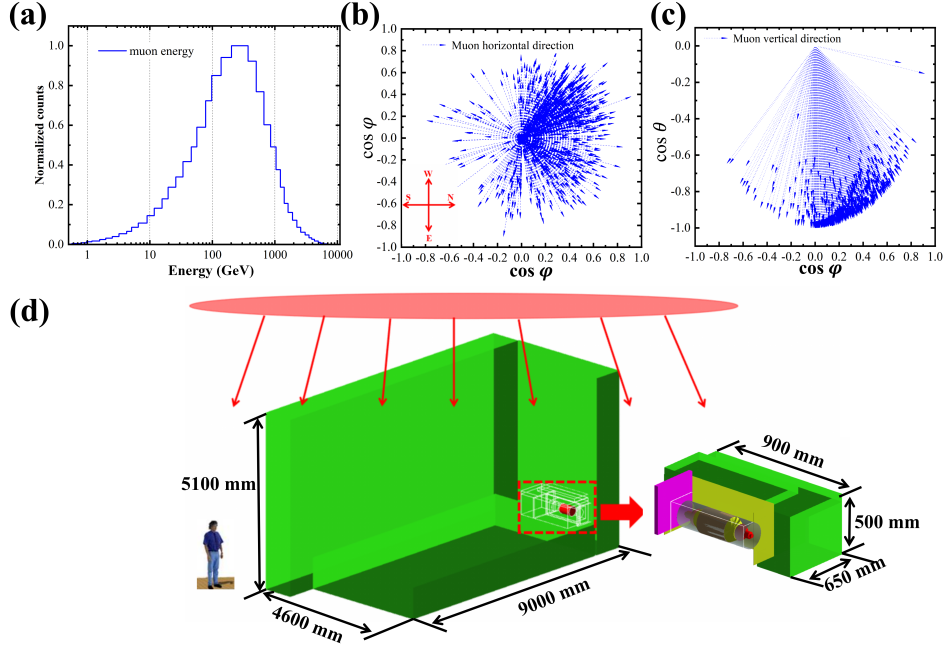
Fig. 4. Particle source and detector simulation modeling used in Geant4 simulation. (a): Muon energy spectrum characterization. (b): Azimuthal distribution of incident muons. (c): Zenith angle distribution of incident muons. (d): Geometric configuration of detector modeling in Geant4.

III. GEANT4 SIMULATIONS OF COSMIC-RAY MUONS AND THEIR DERIVATIVES IN GD-LS DETECTOR

A. Simulation setting

To characterize the composition of 26 saturation events, investigate potential neutron background contributions, calibrate the high-energy response of the detector system, and determine neutron detection efficiency, we implement Monte Carlo simulations using Geant4 (version 4.10.06). In the particle source setup, the GeneralParticleSource in Geant4 is used to generate cosmic-ray muons, with the cosmic-ray muon energy and incidence angle inputs derived from measurements conducted at the China Jinping Underground Laboratory (CJPL) by Guo et al. [13]. The total muon flux is 3.53×10^{-10} cm^{-2}s^{-1} with an average energy of 340 GeV. The distributions of muon energy, azimuthal and zenithal angles are illustrated schematically in Fig. 4 (a), (b) and (c). In addition, the impact of the mountainous structure above the laboratory on the muons has been taken into account through recent measurement [13]. The location of the particle source is illustrated in Fig. 4(d). Muons are generated in a circular plane 5 meters directly above the detector, with a radius of 5 meters. In this configuration, 9,685 muons are emitted in each simulation, corresponding to the number of muon events observed in the PE room over a period of 412 days.

In the detector geometry setup, the detector model is shown in Fig. 4(d). A PE room with dimensions 8 m × 5.6 m × 4.1 m is constructed in the simulation using 1 m thick PE sheets (green squares). The detector is placed in one corner of the room, surrounded by the PE sheets. Additionally, a lead plate shield measuring 0.6 m × 0.6 m × 0.05 m (pink square) is positioned at the front end of the detector, while an aluminum plate shield with a thickness of 0.005 m is placed at both the rear and side (yellow square). The detector body is a cylinder with a diameter of 0.3 m and a length of 0.4 m (brown cylinder), and a PTFE reflective layer (gray cylinder) is applied to the immediate side of the detector. Furthermore, glass light pipes and PMTs are installed on both sides of the detector body in the experimental setup.

B. Simulation of the number of events and deposition energy in detector

To obtain the average number of events for the experiment, more than 3,000 simulations are performed to minimize statistical errors. Consequently, the energy obtained from the simulations is selected, and events with energy deposits smaller than 10 MeV are excluded. The mean number of events yielded by these simulations is 18.55 ± 4.26, which agrees with our reconstructed saturation value of 26 ± 5.10. Furthermore, the 18.55 events obtained from the simulations allow for the identification of particle species. In the simulation, approximately 85% of the events are attributed to cosmic-ray muons, with the remaining 15% being muon-induced electrons. Additionally, it can be postulated that out of the 26 saturated event signals, nearly 22 are caused by cosmic-ray muons, while 4 are caused by muon-induced electrons.

To obtain the energy spectra of cosmic-ray muons and their derivatives in the detector, 9,685,000 cosmic-ray muons are
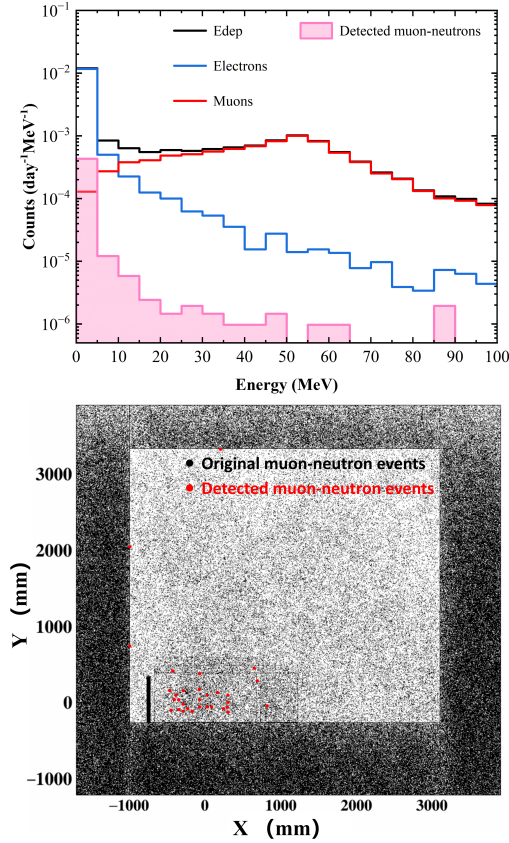
Fig. 5. Energy deposition spectra (top) and two-dimensional distribution of neutron production sites (bottom) within the detector in an experimental environment of more than 1000 years. The black, red, and blue lines in the top illustration represent the total energy deposition of the detector, the energy deposition of muons, and the energy deposition of electrons, respectively. The pink area represents the detected neutron recoil energy. The black dots in the bottom illustration represent the positions where muon neutrons are generated, while the red dots indicate the original positions of the detected neutrons.

produced using a particle source, corresponding to more than 1,000 years of experiments in the same environment. The top inset of Fig. 5 illustrates the energy spectrum obtained from this simulation for energy below 100 MeV in the detector, where the number of counts in the vertical coordinate has been normalized to each day. In the figure, the black solid line represents the total energy deposition in the detector, the red solid line depicts the energy deposition of muon, the blue solid line illustrates the energy contributed by electrons alone, the pink area represents the energy spectrum of neutron recoil nucleus that can be detected in the simulation.

In the energy range above 10 MeV, muon events dominate, with a peak concentration near 53 MeV. This concentration is expected, as muons primarily deposit energy in the detector through ionization, and the energy deposited is directly proportional to the muon's path length. For a detector with a diameter of 30 cm and a length of 40 cm, the average muon path length is approximately 30 cm. Additionally, as anticipated,

a peak appears near 53 MeV, which facilitates the correction of the energy calibration curve during subsequent energy reconstruction. Muon-induced electrons are approximately five times less frequent than muons, with their energy primarily concentrated below 20 MeV.

C. Muon-induced neutrons detection efficiency

This analysis addresses two critical efficiency parameters in neutron detection systems. The neutron detection efficiency (Eff_1) quantifies the probability of neutron capture within the detector volume, defined as the ratio of detected neutrons to incident neutrons. Through Geant4 simulations incorporating the muon-induced neutron energy spectrum from prior measurements as input, 10,000 neutron events yield 3,512 recoil proton events above 10 MeV energy threshold, establishing Eff_1 is 35.1%.

The neutron identification efficiency (Eff_2) characterizes the system's capability to discriminate between muons and muon-induced neutrons above 10 MeV. Signal superposition effects occur when neutron recoil signals coincide temporally with muon signals, causing waveform overlap that compromises PSD effectiveness. We postulate that such superposition events originate from internal neutron recoil processes. Fig. 5 (lower inset) spatially maps simulated neutron detection locations under 1000× magnification, with black markers indicating muon-induced neutron generation points and red markers denoting detected neutron origins. PE shielding effectively attenuates external neutrons, with only 20% of external-origin neutrons penetrating the shielding. These external neutrons exhibit unambiguous detection signatures, achieving 100% identification efficiency. Conversely, 80% of detected neutrons originate internally from muon interactions within the liquid scintillator medium, where simultaneous muon detection complicates identification. Applying the predetermined discrimination threshold (Dis = 0.15), we implement waveform superposition tests: normalized neutron and gamma waveforms are amplitude-scaled (neutron:gamma = 0.75:1 energy ratio) and combined. The composite waveform yields Dis = 0.151, satisfying neutron identification criteria. Simulation data reveal 20.5% of events exceed the 0.75:1 neutron-to-muon energy ratio threshold, which means there is a 20.5% efficiency of distinguishing muon-induced neutrons from muons when both coexist. Combining external neutron detection efficiency (100%) with internal identification efficiency (20.5%) produces the composite neutron identification efficiency Eff_2 is 36.4%

IV. RESULTS

A. Energy spectrum reconstruction of saturated signals

To determine the response of the liquid scintillator as a function of energy, the liquid scintillator detector was calibrated using two gamma sources, ^{137}Cs and ^{60}Co. The energies of the experimental spectral peaks during the energy
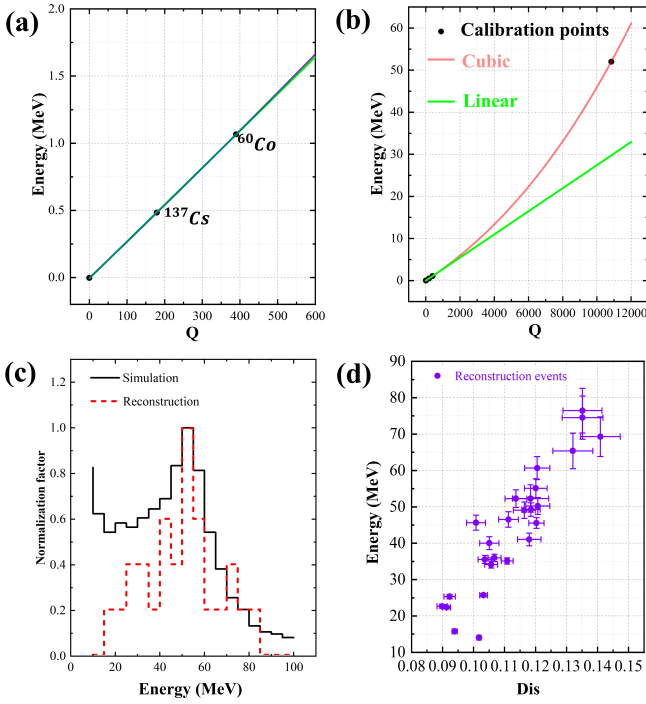
Fig. 6. Results of calibration curve correction and saturation signal events energy reconstruction. (a): Linear calibration in the low-energy regime conducted using ^{137}Cs and ^{60}Co. (b): An additional calibration point is established through comparative analysis between simulated energy spectra and experimental Q-spectra, enabling refinement of the high-energy calibration curve. (c): The reconstructed energy spectrum of the saturation events compared to the simulated energy spectrum. (d): The two-dimensional distribution of energy and Dis of reconstructed saturated events.

calibration process were determined through a combination of experimental measurements and simulation methods, as shown in Fig. 6(a). Nevertheless, the application of linear extrapolation for the calculation of cosmic-ray events may result in a significant bias in the high-energy region (above 10 MeV). In light of these considerations, additional calibration points are incorporated to correct for this bias, and cubic polynomials are used to fit the linear calibration curves. The new calibration points are derived by comparing the peak of the saturation event charge spectrum with that of the simulated energy spectrum. The discrepancy between the three calibration curves is shown in Fig. 6(b). In contrast, the linear fitting and cubic polynomial fitting show a noticeable discrepancy above 5 MeV, leading to a gap of approximately 20 MeV around 50 MeV. The reconstructed energy spectrum of the saturated signal is represented by the red dashed line in Fig. 6(c). The black solid line represents the simulated energy spectrum for energies above 10 MeV. The spectrum is broadened to account for the detector's energy resolution, and the vertical axis is normalized to the respective maxima, showing a reasonable correlation. Furthermore, the expected peak at 50 MeV, indicative of cosmic-ray muons, is clearly visible. Finally, the reconstructed information from the saturated signal events and the calibrated curves is used to reconstruct the Dis and energy data of the saturated signal, as shown in Fig. 6(d).

B. The results of experimental measurement energy spectrum

The PE room at CJPL provides significant neutron shielding, resulting in no cosmic-ray derived neutron events observed in the energy range above 10 MeV during the experimental measurement period of 412 days. The energy spectrum measured in this experiment is shown in Fig. 7. The left panel of Fig. 7 illustrates the combined recoil events from neutrons and background alpha and gamma particles.

The nuclear and alpha recoil events and gamma with energies below 10 MeV are predominantly attributable to the decay of U and Th elements within the surrounding shielding of the detector. The nuclear recoil event with an energy above 10 MeVee is not detected during the 412-day experiment. Nevertheless, through the confidence-level derived from the Poisson distribution and the muon-induced neutron detection efficiency ($Eff_1 \times Eff_2$) discussed earlier, we are able to provide an upper limit for the muon-induced neutron flux of 3.44×10^{-10} cm^{-2} s^{-1} within a 90% confidence-level.

The right panel of Fig. 7 illustrates the energy deposition spectra for muons and electrons. The experimental data points are derived from the reconstruction of 26 saturated signals, while the bar chart represents data from a Geant4 simulation. In the simulation, the energy spectrum is broadened to account for the detector's energy resolution. The experimental results fall within a 2σ range and are slightly higher than the simulated results, indicating that a higher flux is measured in the experiment. Additionally, the best-fitting function is used to estimate the counts of muons and electrons in the dataset. By applying the equation $E_d = a \times E_s$, where E_d represents the experimental energy spectrum and E_s represents the best-fitting simulated spectrum, the value of $a = 1.35 \pm 0.19$ is obtained. The value of E_s is derived from the simulation, allowing the muon and electron counts to be determined. Accordingly, the number of muons and electrons in the experimental data is 21.23 ± 2.99 and 3.75 ± 0.53 per 412 days, respectively. Ultimately, the flux of muons and their induced electrons is $(4.06 \pm 0.57) \times 10^{-10}$ cm^{-2} s^{-1} and $(0.72 \pm 0.1) \times 10^{-10}$ cm^{-2} s^{-1}.

V. SUMMARY

In this study, we report measurements of cosmic-ray muons and their secondary particles, including electrons and neutrons, using a 28-liter Gd-LS detector. A function-fitting method is implemented to reconstruct saturated signal events induced by cosmic-ray muon interactions. These reconstructed events are classified as gamma-like signatures through PSD analysis, exhibiting densely clustered integral values within a characteristic region attributed to muon-induced energy deposition. To determine the detection efficiency of neutrons, refine the detector's energy calibration
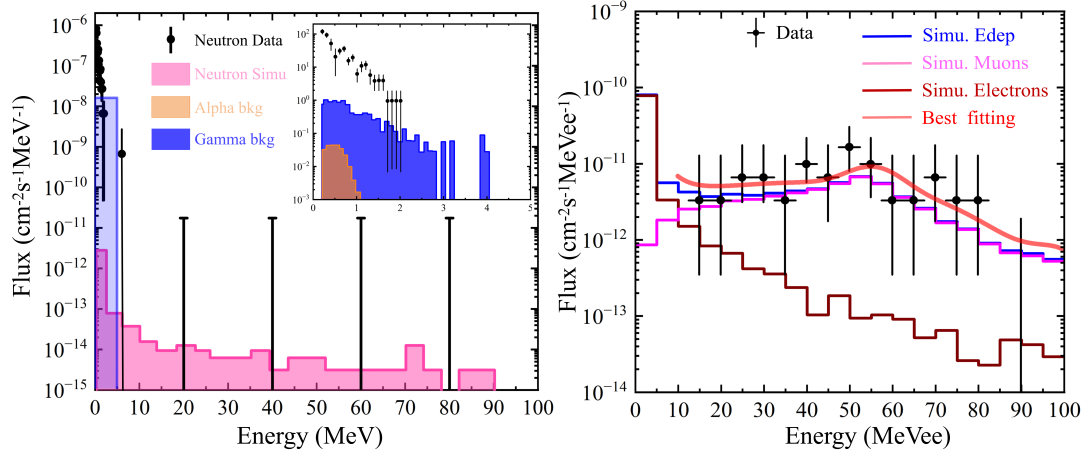
Fig. 7. The left panel depicts the combined recoil signals of neutrons and alpha particles background, with the scatter plot with errors representing the experimental measurement results. The pink, orange and blue areas represent the Geant4 simulation results of neutron, alpha particles recoil and gamma, respectively. The inset shows the events of nuclear recoil energy less than 2 MeV. The right panel depicts the energy deposition signals of muons and electrons. The black data points represent the experimental measurement results, while the blue, pink, and brown bar charts illustrate the total energy spectrum, muons, and electron energy deposition spectrum in Geant4 simulation, respectively. The smooth red curve represents the best fitting result of experimental data.

and resolve ambiguities between muon and electron events, we perform Geant4 simulations incorporating detailed mountain overburden geometry, from which the energy deposition spectra of muons and muon-induced electrons are derived. By simulating the number of neutron events and identifying neutron-gamma mixed waveforms, we obtain a total neutron detection efficiency of 12.8% for the detector. By cross-calibrating the reconstructed saturated events integral spectrum against the simulated energy deposition spectrum, we establish a revised energy-response transfer function for the detector. Through optimally fitting the energy spectra of cosmic-ray muons and muon-induced electrons, we successfully separate muon and electron components in the experimental dataset. In the energy range above 10 MeV, the derived fluxes of cosmic-ray muons and muon-induced electrons are determined as $(4.06 \pm 0.57) \times 10^{-10}$ cm^{-2} s^{-1} and $(0.72 \pm 0.1) \times 10^{-10}$ cm^{-2} s^{-1}, respectively. No muon-induced neutrons are observed, with an upper limit of 3.44×10^{-10} cm^{-2} s^{-1} at a 90% confidence level. The experimental results indicate that the cosmic-ray flux at CJPL is at an exceptionally low level, with the flux of muon-induced neutrons being an order of magnitude lower than that of muons. Therefore, the contribution of muon-induced neutrons in the entire laboratory can be neglected.

VI. BIBLIOGRAPHY

[1] W. P. Liu, Z. H. Li, J. J. he, *et al.*, Progress of Underground Nuclear Astrophysics Experiment JUNA in China, Nuclear Physics News, **63**: 43 (2022). DOI: 10.1007/s00601-022-01735-3

[2] Q. Yue, W. Zhao, K. J. Kang, *et al.*, Limits on light WIMPs from the CDEX-1 experiment with a p-type point-contact germanium detector at the China Jingping Underground Laboratory, Phys. Rev. D, **90**: 091701 (2014). DOI: 10.1103/PhysRevD.90.091701

[3] GERDA Collaboration, GERDA results and the future perspectives for the neutrinoless double beta decay search using ^{76}Ge, Int. J. Mod. Phys. A, **33**: 1843004 (2018). DOI: 10.1142/S0217751X18430042

[4] Stefano Dell' Oro, Simone Marcocci, Matteo Viel, *et al.*, Neutrinoless Double Beta Decay: 2015 Review, Adv. High Energy Phys, **2016**: 2162659 (2016). DOI: 10.1155/2016/2162659

[5] Bhaskar Dutta, Wei Chih Huang, Doojin Kim, *et al.*, Prospects for Light Dark Matter Searches at Large-Volume Neutrino Detectors, Phys. Rep, **133**: 161801 (2024). DOI: 10.1103/PhysRevLett.133.161801

[6] Y. L. Yan, W. X. Zhong, S. T. Lin, *et al.*, Study on cosmogenic radioactive production in germanium as a background for future rare event search experiments, Nuclear Science and Techniques, **31**: 55 (2020). DOI: 10.1007/s41365-020-00762-1

[7] G. Bertone, The moment of truth for WIMP Dark Matter, Nature, **468**: 389-393 (2010). DOI: 10.1038/nature09509

[8] M. Auger, D. J. Auty, P. S. Barbeau, *et al.*, Search for Neutrinoless Double-Beta Decay in ^{136}Xe with EXO-200, Phys. Rev. Lett. **109**: 032505 (2012). DOI: 10.1103/PhysRevLett.109.032505

[9] J. P. Cheng, K. J. Kang, J. M. Li, *et al.*, The China Jin-ping underground laboratory and its early science, Annu Rev Nucl Part Sci, **67**: 231 (2017). DOI: 10.1146/annurev-nucl-102115-044842

[10] K. J. Kang, J. P. Cheng, Y. H. Chen, *et al.*, Status and prospects of a deep underground laboratory in China, Phys.: Conf. Ser,

203: 012028 (2010). DOI: 10.1088/1742-6596/203/1/012028

[11] B. Aharmim, S. N. Ahmed, T. C. Andersen, *et al*., Measurement of the cosmic ray and neutrino-induced muon flux at the Sudbury neutrino observatory, Phys. Rev. D, **80**: 012001 (2009). DOI: 10.1103/PhysRevD.80.012001

[12] Y. C. Wu, X. Q. Hao, Q. Yue, *et al*., Measurement of cosmic ray flux in the China JinPing underground laboratory, Chinese Physics C, **37**: 086001 (2013). DOI: 10.1088/1674-1137/37/8/086001

[13] Z. Y. Guo, Lars Bathe Peters1, S. M. Chen, *et al*., Muon flux measurement at China Jinping Underground Laboratory, Chinese Physics C, **45**: 025001 (2021). DOI: 10.1088/1674-1137/abccae

[14] V. A. Kudryavtsev, L. Pandola and V. Tomasello, Neutron- and muon-induced background in underground physics experiments, Eur. Phys. J, **36**: 171 (2008). DOI: 10.1140/epja/i2007-10539-6

[15] Q. Du, S. T. Lin, S. K. Liu, , *et al*., Measurement of the fast neutron background at the China Jinping Underground Laboratory, Instrum. Meth. A, **889**: 105-112 (2018). DOI: 10.1016/j.nima.2018.01.098

[16] M. B. Gromov, D. S. Kuznetsov, A. E. Murchenko, *et al*., Stability of Gadolinium-Doped Liquid Organic Scintillators, Technical Physics Letters, **44**: 251-254 (2018). DOI: 10.1134/S1063785018030185

[17] Q. Du, S. T. Lin, H. T. He, *et al*., Response of gadolinium doped liquid scintillator to charged particles: measurement based on intrinsic U/Th contamination, JINST, **13**: P04001 (2018). DOI: 10.1088/1748-0221/13/04/P04001

[18] W. X. Zhong, C. H. Fang, S. T. Lin, *et al*., Identification of neutron sources and background levels in the polyethylene room of the China Jinping Underground Laboratory, JINST, **16**: P12003 (2021). DOI: 10.1088/1748-0221/16/12/P12003

[19] S. X. Liu, W. Zhang, Z. H. Zhang, *et al*., Performance of real-time neutron/gamma discrimination methods, Nuclear Science and Techniques, **34**: 8 (2023). DOI: 10.1007/s41365-022-01160-5

[20] J. X. Li, H. L. Hou, Y. F. Huang, *et al*., Pulse-shaping method for real-time neutron/gamma discrimination at low sampling rates, Nuclear Science and Techniques, **34**: 165 (2023). DOI: 10.1007/s41365-023-01306-z

[21] Z. M. Zeng, H. Gong, Q. Yue, *et al*., Thermal neutron background measurement in CJPL, Nucl. Instrum. Meth. A, **804**: 108 (2015). DOI: 10.1016/j.nima.2015.09.043

[22] Y. W. Hu, H. Y. Jiang, Z. Q. Cui, *et al*., Simulation method for measurement of the cross-section of the 14N(n, α)11B reaction using a gridded ionization chamber, Nuclear Science and Techniques, **32**: 78 (2021). DOI: 10.1007/s41365-021-00921-y

[23] Y. T. Li, W. P. Lin, B. S. Gao, *et al*., Development of a low-background neutron detector array, Nuclear Science and Techniques, **33**: 41 (2022). DOI: 10.1007/s41365-022-01030-0

[24] Q. Xiao, J. H. Cheng, Y. Y. Xu, *et al*., α Decay in extreme laser felds within a deformed Gamow-like model, Nuclear Science and Techniques, **35**: 27 (2024). DOI: 10.1007/s41365-024-01371-y

[25] Dejan Jokovic, Dimitrije Maletic, Aleksandar Dragic, *et al*., Application of Geant4 simulation in measurement of cosmic-ray muon flux and studies of muon-induced background, Eur. Phys. J. Plus, **138**: 1006 (2023). DOI: 10.1140/epjp/s13360-023-04639-1

[26] L. X. Zhang, S. Z. Chen, Z. D. Zhang, *et al*., Resolution analysis of thermal neutron radiography based on accelerator-driven compact neutron source, Nuclear Science and Techniques, **34**: 76 (2023). DOI: 10.1007/s41365-023-01227-x

[27] H. Park, J. Kim, Y. Hwang, *et al*., Neutron spectrum at the underground laboratory for the ultra low background experiment, Appl. Radiat. Isot, **81**: 302-306 (2013). DOI: 10.1016/j.apradiso.2013.03.068

[28] Bhaskar Mukherjee, A novel neutron energy spectrum unfolding tool using a genetic algorithm, Nucl. Instrum. Meth. A, **432**: 305 (1999). DOI: 10.1016/S0168-9002(99)00535-5

[29] W. Chen, L. Ma, J. H. Chen, *et al*., Gamma-, neutron-, and muon-induced environmental background simulations for 100Mo-based bolometric double-beta decay experiment at Jinping Underground Laboratory, Nuclear Science and Techniques, **34**: 135 (2023). DOI: 10.1007/s41365-023-01299-9

[30] Y. Xu, Y. S. Ning, Z. Z. Qin, *et al*., Development of a scintillating-fber-based beam monitor for the coherent muon-to-electron transition experiment, Nuclear Science and Techniques, **35**: 79 (2024). DOI: 10.1007/s41365-024-01442-0

[31] A. Bettini, Underground laboratories, Nuclear Instruments and Methods in Physics Research A, **626-627**: S64-S68 (2011). DOI: 10.1016/j.nima.2010.05.017

[32] GEANT4 collaboration, GEANT4–a simulation toolkit, Nucl. Instrum. Meth. A, **506**: 250-303 (2003). DOI: 10.1016/S0168-9002(03)01368-8

[33] Q. D. Hu, H . Ma, Z. Zeng, *et al*., Neutron background measurements at China Jinping underground laboratory with a Bonner multi-sphere spectrometer, Nucl. Instrum. Meth. A, **859**: 37-40 (2017). DOI: 10.1016/j.nima.2017.03.048

[34] Y. Liu, J. J. Zhu, Neil Roberts, *et al*., Recovery of saturated signal waveform acquired from high-energy particles 0with artificial neural networks, Nuclear Science and Techniques, **30**: 30 (2019). DOI: 10.1007/s41365-019-0677-0

[35] B. Mahmoodzadeh Vaziri, A. Shahsavand, Analysis of supersonic separators geometry using generalized radial basis function(GRBF) artificial neural networks, Nucl. Instrum. Meth. A, **13**: 30-41 (2013). DOI: 10.1016/j.jngse.2013.03.004